Structural Chemistry (2024) 35:1059–1073
https://doi.org/10.1007/s11224-024-02330-4

RESEARCH

Effects of graphene and thermoplastic elastomer on tailoring the bulk properties of asphaltenes: an exploration from classical and quantum simulations

Pabitra Narayan Samanta[1] · Devashis Majumdar[1] · Jerzy Leszczynski[1]

Received: 25 March 2024 / Accepted: 17 April 2024 / Published online: 30 April 2024

Abstract
The modulation of bulk properties including the cohesive strength and the solubility of the asphaltenes, due to the inclusion of graphene nanosheets and the thermoplastic polymer, is probed by performing all-atom classical molecular dynamics (MD) simulations. The impact of morphological heterogeneity, including the size of the aromatic core of the asphaltene molecule, the nature of the heteroatom attached to the aromatic core, the orientation of the graphene nanosheets, and the surface area of the nanomaterial, on the bulk properties of the model systems of nanocomposites and interfaces is explored. The cohesive strength of the asphaltene composites is significantly enhanced by the introduction of graphene nanosheets. The addition of styrene–butadiene–styrene (SBS) block copolymer into the graphene-reinforced asphaltene systems improves the cohesive strength, structural plasticity, and compatibility between the nanomaterial and the asphaltenes. The π–π stacking interaction between the graphitic surface and the aromatic core of the asphaltene is identified to be the major driving force for modulating the cohesive strength. The dispersion interaction maximizes in the hierarchical layered structure compared to the randomly oriented structure of the graphene nanosheets and the asphaltene molecules. The energetics of non-covalent interaction are further assessed within the framework of dispersion-corrected density functional theory (DFT)-based methods. The DFT-derived adsorption energies and thermochemical properties substantiate the stronger interaction and the thermodynamic favorability of the adsorption processes in both the gas phase and solvent medium (toluene). The simulated IR and Raman spectra are also analyzed to reveal the nature of the interaction.

Keywords Graphene · Asphaltenes · SBS · Cohesive energy · Solubility · IR and Raman spectra

Introduction

Asphaltene is one of the key components of asphalt and is identified as an intricate and multifaceted combination of heavy organic molecules with an average molecular weight of around 750 Da as determined by mass spectrometric and time-resolved fluorescence depolarization measurements [1, 2]. However, a precise estimation of the molecular structures as well as molecular masses of the asphaltenes is an ongoing challenge because of their diversity of chemical composition and they tend to form nanoaggregates in reservoir crude oil as well as in solvents that are used for experimental laboratory [3–5]. Asphaltenes are classified as polycyclic aromatic hydrocarbons (PAHs) that have a naturally occurring graphitic structure. The graphitic structure leads to the formation of asphaltene aggregates driven by π–π stacking interactions of the aromatic cores, evidenced by the previous experimental measurements including X-ray diffraction and Raman spectroscopy [6–8]. Although the core structure of the asphaltenes is commonly described by medium to large PAHs (typically 4–10 aromatic rings), the asphaltene molecules also contain aliphatic chains with a length of three to seven carbon atoms, polar functional groups, and heteroatoms (N, O, and S) at a reduced level [9–11]. Asphaltene molecules are usually insoluble in n-alkanes, such as n-heptane and n-pentane, but they can be dissolved in aromatic solvents like toluene and benzene [1]. The viscosity of heavy oil is closely related to its asphaltene content, which is an essential factor to consider in the oil industry. The behavior of asphaltene molecules in terms of aggregation is solely responsible for the deposition,

✉ Jerzy Leszczynski
jerzy@icnanotox.org

[1] Center for Computational Chemistry, Department of Chemistry, Physics and Atmospheric Sciences, Jackson State University, Jackson, MS 39217, USA

emulsification, and high viscosity of heavy oil [12]. This has a significant impact on the utilization and value of heavy oil, making it vital to study asphaltene and its behavior.

Unraveling the chemical structure of the asphaltene molecules and the factors responsible for their aggregation in crude oil and laboratory solvents has been the focus of extensive research for optimizing the refinery process of heavy oil. To date, numerous experimental studies [1, 12] utilizing a variety of characterization techniques, such as spectroscopy, diffraction, microscopy, and chromatography, as well as theoretical investigations [11, 13–27] employing ab initio quantum chemical methods and classical molecular dynamics (MD) simulations, have been carried out to explore the structure and physicochemical properties of asphaltenes. As revealed by these previous in-depth analyses, the molecular models of asphaltenes could be exemplified by three plausible chemical network structures, viz., island, archipelago, and aryl-linked structures. The island structure is characterized by the existence of a central aromatic core with fused aromatic rings surrounded by aliphatic groups. In the case of archipelago model structures, several distinct polycyclic aromatic/heteroaromatic cores are connected by saturated alkyl bridges. Like the island model, the aryl-linked structure also comprises a single aromatic core; however, the adjacent aromatic ring systems are not entirely fused. Such an aryl-linked structure contains one or more aryl linkages between aromatic moieties. Furthermore, all kinds of asphaltenes undergo aggregation that depends on several factors including the aromaticity of the graphitic network, the length and polarity of the aliphatic chains, the existence of heteroatoms, and other fluidic properties such as temperature, pressure, and the type of solvent. However, the mechanistic details of the asphaltene aggregation phases starting from nanoaggregate (typically comprised of ~ 6–7 asphaltene molecules attaining a size of ~ 2 nm) to cluster formation (consisting of ~ 8 nanoaggregates producing a length scale of ~ 5 nm) are debatable. In this regard, two distinct models covering the modified Yen–Mullins model and the supramolecular structural model are widely recognized to elucidate the propensity of self-interaction and self-assembly of asphaltenes. As hypothesized by the Yen–Mullins model [9, 10], the growth of asphaltene nanoaggregates and clusters is crucially facilitated by the π–π interactions between the aromatic cores, and the extent of aggregation is constrained by the steric hindrance stemming from the aliphatic side chains. On the other hand, as outlined by Gray et al. [28], the consideration of aromatic stacking interactions exclusively cannot explain the substantial experimental findings including the complexity of asphaltene molecular structure (e.g., the existence of carboxylic acids/esters, nitrogen bases, porphyrins), the coagulation behavior of the aggregates, occlusion characteristics of asphaltene aggregates, the presence of porosity within the asphaltene aggregates, the formation of viscoelastic films at the oil–water interface, and the factors influencing the mechanical responses and the chemical behavior of the asphaltene aggregates for interacting with resins and surfactants. To resolve the shortcomings of the Yen–Mullins model, Gray et al. [28] introduced an alternative model that focuses on the supramolecular assembly of asphaltene molecules. This model helps to rationalize the formation of aggregates/clusters that are assisted by cooperative binding involving acid–base interactions, hydrogen bonding, hydrophobic interactions, coordination to metal complexes, and π–π aromatic stacking.

The seamless growth of asphaltene nanoaggregates and clusters followed by the progression of bulk phase separation of the asphaltenes caused by the inclusion of exorbitant asphaltenes/solutes or by the attenuation of asphaltene solvency can lead to various issues in oil production and transportation, including pipeline and wellbore blockages, fouling and corrosion of equipment, and formation of stable oil–water emulsions [29–31]. To alleviate these problems, a multitude of research works has been carried out to assess the efficacy of diverse nanomaterials starting from inorganic nanoparticles to carbon-based nanostructures and polymers for asphaltene adsorption and oil demulsification [32–43]. In an earlier experimental study [44], it was demonstrated that the asphaltene adsorption capacity reaches the maximum for the reduced graphene oxide (rGO) compared to the other carbon-based nanomaterials including multiwall carbon nanotubes (MWCNTs), carbon black (CB), and activated carbon (AC). The adsorption affinity of the carbonaceous adsorbents toward the asphaltene molecules follows the trend: rGO > MWCNTs > CB > AC. The attainability of stronger π–π interactions and the availability of larger surface area are suggested to be the predominant factors for enhancing the asphaltene adsorption capacity of rGO and MWCNTs. Moreover, the asphaltene adsorption capacity is modulated by the alteration of heptane content; however, the loading capacity of the adsorbents is not impacted by the water content. The predicted thermodynamic parameters manifest that the adsorption of asphaltenes on the carbon-based nanostructures is exothermic and spontaneous. The atomic-scale mechanism of destabilization of oil–water emulsions by adding GO into the model systems of asphaltenes was further explored via MD simulations [45].

Stimulated by the affirmative consequences of the inclusion of carbon-based nanomaterials, especially rGO, in modulating the asphaltene adsorption capacity, the present computational study focuses on estimating the role of the structural building block of the asphaltene molecules toward the adsorption affinity of graphene-based nanostructures. Regardless of elucidating the asphaltene aggregation and cluster formation, we emphasize determining the critical factors contributing to the interfacial interaction due to the alteration of the aromatic core of the asphaltene molecules decorated by a heteroatom and the inclusion of size effects of the graphene nanosheets. The compatibility between asphaltenes and graphene fillers has been assessed

by analyzing the cohesive energy, heat of formation, and solubility parameters from the ensemble-averaged structures as acquired by classical MD simulations. The impact of the addition of block copolymers such as styrene–butadiene–styrene (SBS) on the microstructure and solubility properties of the graphene-modified asphaltenes is further assessed. The introduction of SBS copolymer was demonstrated to be an effective strategy for improving the thermo-rheological behavior of the asphalt and modifying the asphalt emulsion [46–48]. The essence of interfacial interactions is additionally estimated from the finite model of the robust graphene-asphaltene system by computing adsorption energy, thermochemical properties, IR stretching frequencies, and Raman scattering activities, within the framework of density functional theory (DFT). The stability of the graphene-asphaltene composite in the presence of an aromatic solvent (e.g., toluene) is also examined by evaluating the adsorption energy and thermochemical properties with the aid of the DFT-based polarizable continuum model (PCM).

Computational details

MD simulation of graphene-asphaltene systems

To explore the microstructure and energetics of the graphene-modified asphaltene systems, we have chosen three distinct asphaltene molecules comprising heteroatoms (S, N, and O) within the graphitic network structure, which are designated as A1, A2, and A3. The model systems were constructed based on the Yen–Mullins model and utilized previously as members of asphaltenes to investigate the properties of asphalt [49–54]. In an earlier theoretical study [13], it was demonstrated that the association free energy of the asphaltene molecules is significantly influenced by the presence of heteroatom on the aromatic core compared to the existence of heteroatom on the aliphatic chains. Furthermore, the asphaltene dimerization is not impacted by the length and number of the aliphatic chains even though the size of the asphaltene aggregates is affected by the aliphatic chains attached to the aromatic core. The interaction between the aromatic cores of the asphaltene molecules is shown to be the key force for their association. Thus, to estimate the theoretical maximum limit of the interaction energy between the graphene surface and the asphaltene molecules as well as to reduce the computational cost, the model systems of the asphaltene molecules are further simplified by excluding the aliphatic chains from the aromatic core. Figure 1 shows the 3D representation of the chemical structure of the asphaltenes considered for the present computational study. To predict the influence of heteroaromatic core on the asphaltene adsorption capacity of the graphene nanostructure, the model systems of the graphene-asphaltene nanocomposites were generated by adding 60 asphaltene molecules and 8 graphene nanosheets to the simulation box. The structural details of the graphene-asphaltene nanocomposites considered for the MD simulation study are further provided in Table 1. To resolve the finite size effects of the graphene nanosheet (GNS) in characterizing interfacial interaction with the asphaltenes, the hierarchical models of graphene-asphaltene nanocomposites were further generated by adding 64 asphaltene molecules to the cell comprising two bilayer-GNS. Notably, bonds between the primary and neighboring cells, i.e., image bonds were invoked for simulating the asphaltene matrix with the periodic multilayered graphene nanosheet (PMG). The structural parameters of the simulation cell corresponding to the hierarchical models of graphene-polymer nanocomposites are shown in Table 2. To explore the impact of copolymer on the asphaltene adsorption capacity and the solubility of the nanocomposites, the SBS polymer chains with 200 carbon atoms were further added to each graphene-asphaltene model system. All the model systems were constructed using the Disordered System Builder utility of the Schrödinger Material Science suite release 2020–4 (Schrödinger, LLC, New York, NY, 2020).

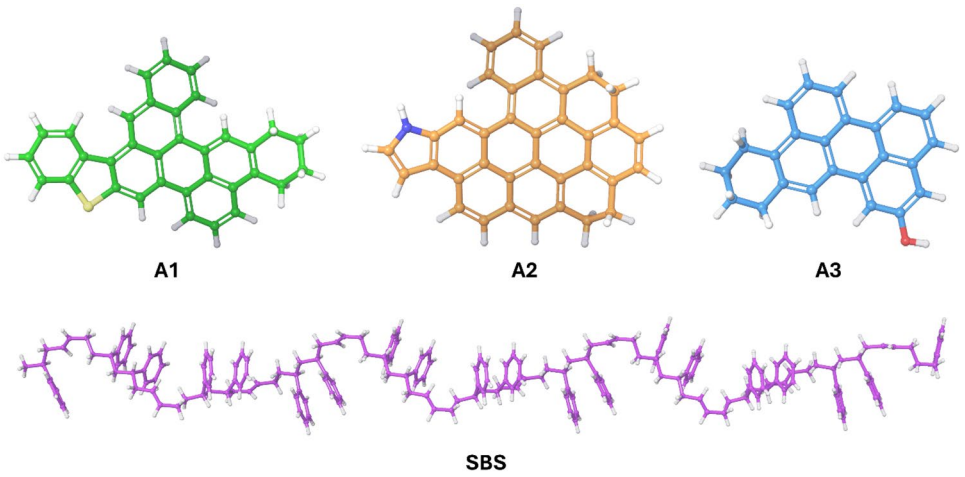

Fig. 1 Representation of chemical structures of the asphaltene molecules and styrene–butadiene–styrene (SBS) block copolymer used for the construction of model systems of nanocomposites and interfaces

Table 1 Structural details of simulated systems of nanocomposites comprising asphaltenes, graphene nanosheets (GNS), and SBS block copolymer

System	Component	Chemical Formula	No. of Molecules	Total No. of Atoms	Total Mass (amu)	Final volume (Å^3)
Asphaltene1	A1	$C_{34}H_{22}S$	60	3420	27,757.106	39,019.31
Asphaltene2	A2	$C_{36}H_{21}N$	60	3480	28,054.528	37,676.06
Asphaltene3	A3	$C_{24}H_{18}O$	60	2580	19,344.628	26,864.79
GNS-A1	A1	$C_{34}H_{22}S$	60	4540	38,568.831	50,475.21
	GNS	$C_{110}H_{30}$	8			
GNS-A2	A2	$C_{36}H_{21}N$	60	4600	38,866.253	49,671.38
	GNS	$C_{110}H_{30}$	8			
GNS-A3	A3	$C_{24}H_{18}O$	60	3700	30,156.352	38,188.50
	GNS	$C_{110}H_{30}$	8			
GNS-A1/SBS	A1	$C_{34}H_{22}S$	92	8052	63,876.619	87,885.35
	GNS	$C_{110}H_{30}$	8			
	SBS	$C_{200}H_{222}$	4			
GNS-A2/SBS	A2	$C_{36}H_{21}N$	92	8144	64,332.665	85,838.81
	GNS	$C_{110}H_{30}$	8			
	SBS	$C_{200}H_{222}$	4			
GNS-A3/SBS	A3	$C_{24}H_{18}O$	92	6764	50,977.484	69,649.96
	GNS	$C_{110}H_{30}$	8			
	SBS	$C_{200}H_{222}$	4			

To perform all-atom classical MD simulations, we have employed the optimized OPLS4 force field parameters [55] for all the systems. To commensurate simulation box size and achieve a system with the desired density, each model system was fully relaxed before the execution of production MD simulation under the isothermal-isobaric (NPT) ensemble. The relaxation protocol consists of 20 ps of Brownian dynamics within the isothermal-isochoric (NVT) ensemble at 10 K, followed by 20 ps of Brownian dynamics under the NPT ensemble at 100 K, and 100 ps of MD under the NPT ensemble at 300 K. Subsequently, each system was equilibrated by executing 10 ns of MD simulation

Table 2 Structural details of simulated systems of interfaces comprising asphaltenes, periodic multilayered graphene nanosheets (PMG), and SBS block copolymer

System	Component	Chemical formula	No. of molecules	Total no. of atoms	Total mass (amu)	Final volume (Å^3)
PMG-A1	A1	$C_{34}H_{22}S$	64	5952	57,281.270	62,141.67
	PMG	C_{576}	4			
PMG-A2	A2	$C_{36}H_{21}N$	64	6016	57,598.520	60,740.08
	PMG	C_{576}	4			
PMG-A3	A3	$C_{24}H_{18}O$	64	5056	48,307.959	49,794.79
	PMG	C_{576}	4			
PMG-A1/SBS	A1	$C_{34}H_{22}S$	60	7412	65,934.793	77,234.59
	PMG	C_{576}	4			
	SBS	$C_{200}H_{222}$	4			
PMG-A2/SBS	A2	$C_{36}H_{21}N$	60	7472	66,232.215	77,891.91
	PMG	C_{576}	4			
	SBS	$C_{200}H_{222}$	4			
PMG-A3/SBS	A3	$C_{24}H_{18}O$	60	6572	57,522.315	64,964.45
	PMG	C_{576}	4			
	SBS	$C_{200}H_{222}$	4			

under the NPT ensemble. After equilibration, a production MD run was performed for 200 ns for each nanocomposite. A Nose–Hoover chain thermostat [56–58] with a relaxation time of 1 ps was used to keep the temperature at 300 K. For performing the simulations at the NPT ensemble, we have employed Martyna-Tobias-Klein (MTK) barostat [59] with a relaxation time of 2 ps to restrict the pressure fluctuation at 1.01325 bar. The NPT MD simulations of the nanocomposites comprising finite GNS were performed using the isotropic pressure coupling, while the semi-isotropic pressure coupling was employed for simulating the hierarchical model systems comprising PMG. Periodic boundary conditions (PBC) were applied to represent a bulk amorphous phase of the asphaltene-graphene systems. The MD simulations were performed using the multistage simulation workflow of the Desmond code on GPU (Schrödinger Release 2020–4: Desmond Molecular Dynamics System, D. E. Shaw Research, New York, NY, USA, 2020. Maestro-Desmond Interoperability Tools, Schrödinger, New York, NY, USA, 2020) [60].

DFT computations on graphene-asphaltene composite

To demonstrate the nature of non-covalent interactions more precisely, the quantum chemical calculations are further conducted for the strongly adsorbed graphene-asphaltene system as predicted from classical MD simulations of the nanocomposites. The structure and energetics of the molecular models of the graphene-asphaltene composite were derived from the DFT calculations using the B3LYP hybrid exchange–correlation functional [61–63] and the 6-31G(d) basis sets for all the atoms involved in the composite. Dispersion corrections were added to the self-consistent electronic energy through Grimme's D3 correction method together with Becke-Johnson damping (GD3BJ) [64]. The ground state geometry of the pristine materials and their adsorbed complex was obtained by performing full structural relaxation of the model systems without imposing any symmetry constraints. During the geometry optimization, the SCF convergence criteria on both energy and density were set to 10^{-6} a.u. To verify the critical point on the potential energy surface (PES) that refers to the equilibrium geometry, the harmonic stretching frequencies of the normal modes were analyzed for the relaxed structures of the graphene-asphaltene system. Next, to assess the binding strength between the asphaltene molecule and the GNS in the presence of an aromatic solvent, the molecular geometries were reoptimized in an implicit solvent medium of toluene (dielectric constant, $\varepsilon = 2.374$), and the harmonic stretching frequency analyses were performed to locate the global minima structure on the PES. The electronic energies of the asphaltene molecule, GNS, and the GNS-asphaltene complex in the solvent phase were derived from the DFT-based self-consistent reaction field (SCRF) calculations within the framework of integral-equation-formalism polarizable continuum model (IEF-PCM) [65–67]. All DFT calculations were carried out using the Gaussian 16 suite of programs [68].

Results and discussion

To weigh the performance of the force field parameters and the simulation workflows considered for the present computational study, the predicted bulk properties of the pristine asphaltene systems are critically analyzed and compared with prior research data. The equilibrium geometries of the model systems of asphaltene composites extracted from the 200 ns production NPT MD runs are delineated in Fig. 2. First, we probe the density of the model systems of asphaltene molecules calculated for each frame throughout the 200 ns period of NPT MD simulations. The computed average (Avg) density at 300 K along with the standard deviation (SD) of the mean value has been displayed in Table 3 for each asphaltene system. The calculated ensemble-averaged density values vary between 1.18 and 1.24 g/cm^3. Noticeably, the density value alters with the size of the aromatic core and the nature of the heteroatom (e.g., S, N, or O) attached to the aromatic core of the asphaltene molecule, and it reaches the maximum for the A2 structure comprising N-substituted aromatic moiety. The calculated densities for distinct asphaltene model systems corroborate well with the experimentally measured values ranging from 1.16 to 1.25 g/cm^3 [69]. To examine the conformational stability of the simulated systems, the evolution of the density of the asphaltene systems as a function of simulation time is depicted in Figs. S1–S3. The reliability of the MD trajectory for further dynamic event analyses and the equilibration of the simulated systems are substantiated by the steady fluctuation of the densities over coordinates for studied asphaltene systems comprising A1, A2, and A3 molecules, respectively.

To evaluate the strength of intermolecular interaction between the aromatic cores of the asphaltenes and the impact of their structural building block on the degree of solubility, we have analyzed the Hildebrand solubility parameter (δ_{Hild}) which is related to the cohesive energy (E_{coh}) of a condensed-phase molecular system [70]

$$\delta_{Hild} = \sqrt{\frac{E_{coh}}{V_m}} = \sqrt{\frac{\Delta H_{vap} - RT}{V_m}}$$

where V_m denotes the molar volume, R is the gas constant, and T is the temperature. ΔH_{vap} refers to the heat of vaporization which can be calculated as,

$$\Delta H_{vap} = \langle E_{cell} - \sum_{i=1}^{N} E_i \rangle_P + RT$$

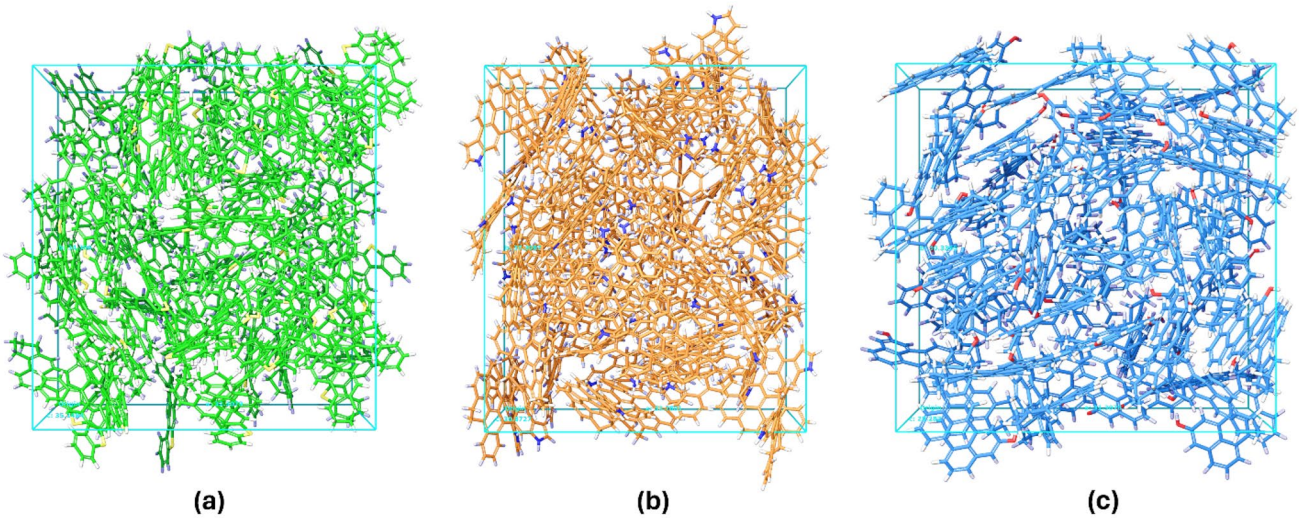

Fig. 2 Equilibrium geometries of the composites consisting of **a** A1, **b** A2, and **c** A3 asphaltene molecules, as extracted from the 200 ns NPT MD simulations

where E_{cell} is the total energy of the system, and E_i corresponds to the energy of the individual molecule. The brackets $\langle \dots \rangle_P$ indicate an average over the P time samples, i.e., the MD trajectory acquired from the simulations under the NPT ensemble. The computed E_{coh}, ΔH_{vap}, and δ_{Hild} for the three asphaltene systems are provided in Table 3. As revealed by the calculated data, both the ΔH_{vap} and E_{coh} show a strong dependence on the model structure of the asphaltene and follow the trend: A2 > A1 > A3. Notably, the value of E_{coh} increases with increasing the aromatic core size which in turn augments the π–π stacking interaction. Moreover, the relative change in E_{coh} firmly supports the predicted trend in the density of the asphaltene systems. Although the E_{coh} gets stronger in the case of the A2 molecule, the solubility of the studied asphaltene systems obeys the order: A3 > A2 > A1. The enhanced solubility of the A3 crucially arises from the smaller molecular size compared to the A2 and A1, while the order of solubility is predominantly guided by the increment of E_{coh} for the A2 and A1.

To determine the contribution of polar, dispersion, and hydrogen bond interactions toward the enhancement of the solubility of asphaltenes, we emphasize the estimation of Hansen solubility parameters. An extension of the Hildebrand solubility parameter was proposed by Hansen [71], to assess the relative miscibility of polar and hydrogen bonding systems,

$$\delta^2 = \delta_d^2 + \delta_p^2 + \delta_h^2$$

where δ_d, δ_p, and δ_h correspond to the dispersion, electrostatic, and hydrogen bond components of δ, respectively. The components could be computed from the MD average potential energy components of the condensed phase simulation,

$$\delta_k^2 = \left(\frac{\sum_{i=1}^{n} \langle E_i^k - E_c^k \rangle}{N_0 \langle V_c / n \rangle}\right)$$

where E_c^k represents the total non-covalent energy of the simulated system, E_i^k refers to the energy components of the individual molecules, V_c denotes the volume of the simulated sample, the brackets $\langle \dots \rangle$ define a time average quantity over the duration of the MD, n represents the number of molecules, k accounts for the coulomb (polar), van der Waals

Table 3 Comparison of estimated ensemble-averaged bulk properties of the asphaltene composites as extracted from the 200 ns production MD runs under NPT ensemble

Composites		ρ (g/cm^3)	E_{coh} (kcal/mol)	δ_{Hild} (MPa)$^{1/2}$	$\delta_{Han/vdW}$ (MPa)$^{1/2}$	$\delta_{Han/Elec}$ (MPa)$^{1/2}$	ΔH_{vap} (kcal/mol)
A1	Avg	**1.18**	**35.18**	**19.39**	**18.87**	**4.45**	**35.78**
	SD	0.007	0.248	0.112	0.117	0.133	0.248
A2	Avg	**1.24**	**38.76**	**20.71**	**19.51**	**6.94**	**39.36**
	SD	0.006	0.233	0.100	0.099	0.100	0.233
A3	Avg	**1.20**	**31.14**	**21.98**	**19.78**	**9.59**	**31.73**
	SD	0.006	0.255	0.128	0.115	0.171	0.255

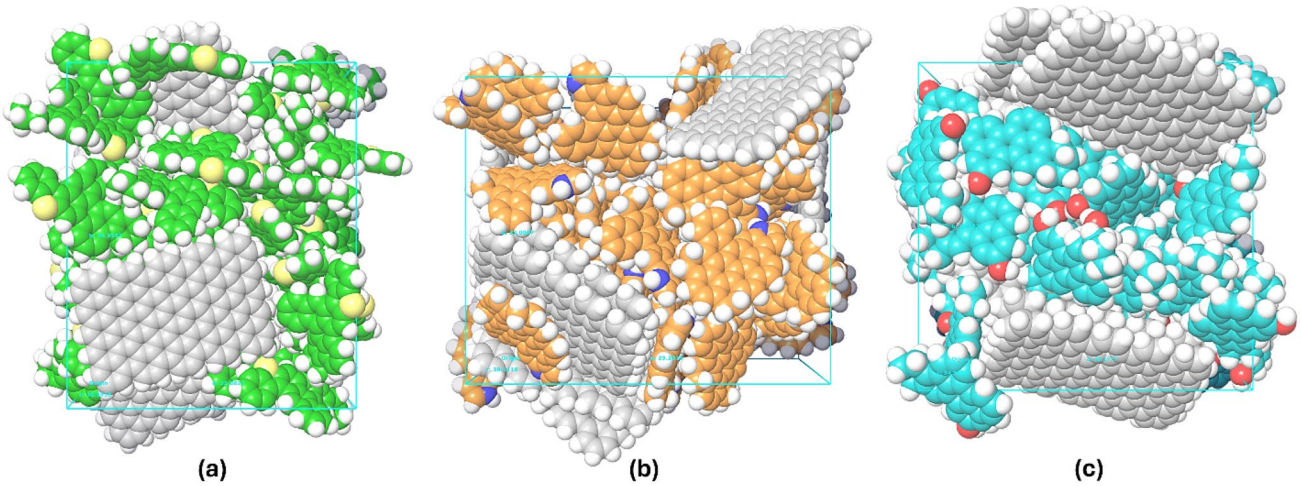

Fig. 3 Equilibrium geometries of the nanocomposites comprising graphene nanosheets (GNS) and asphaltene molecules: **a** GNS-A1, **b** GNS-A2, and **c** GNS-A3, as extracted from the 200 ns NPT MD simulations

(dispersion) and hydrogen bond components, respectively, and N_0 refers to Avogadro's number. As evidenced by the calculated coulomb ($\delta_{Han/Elec}$) and van der Waals ($\delta_{Han/vdW}$) counterparts of the Hansen solubility parameter displayed in Table 3, the intermolecular interactions are chiefly controlled by the vdW forces. The dispersion component δ_d of the Hansen solubility parameter (which is represented by $\delta_{Han/vdW}$ in the present study) is predicted to be 18.87, 19.51, and 19.78, respectively, for the A1, A2, and A3. The calculated δ_d values are very close to the previously measured value of 19.6 for the asphaltenes as derived from the Venezuelan bitumen [72, 73].

Next, the binding strength between the GNS and the asphaltene molecules is probed by analyzing the 200 ns NPT MD trajectory of the GNS-asphaltene nanocomposites. The thermally equilibrated structures of the GNS-asphaltene nanocomposites produced after the accomplishment of production MD runs are shown in Fig. 3. The calculated ensemble-averaged bulk properties for each nanocomposite are provided in Table 4. Due to the incorporation of GNS into the simulation cell comprising asphaltene molecules, the density of the nanocomposites is enhanced by 0.06–0.11 g/cm^3 compared to the pristine asphaltene composites. The E_{coh} of the graphene-modified asphaltene systems, viz., GNS-A1, GNS-A2, and GNS-A3, are elevated by about 9.2 kcal/mol, 7.8 kcal/mol, and 10.1 kcal/mol, respectively, with respect to the parent asphaltene composite. However, the predicted trends in ΔH_{vap} and E_{coh} are in consistent with the order obtained for pristine asphaltene systems: GNS-A2 > GNS-A1 > GNS-A3. As evidenced by the computed Hildebrand solubility parameter, the solubility of the GNS-A1, GNS-A2, and GNS-A3 nanocomposites is escalated by 5.05%, 1.59%, and 2.72%, respectively, relative to the pure substances. The calculated Hansen solubility parameters manifest that the formation of graphene-asphaltene nanocomposites is primarily assisted by the dispersion interactions. Furthermore, the contribution of the dispersion component to the solubility is uplifted by 4.25–7.74% for the graphene-modified asphaltene systems, while the polar part is reduced by 1.12–2.12 $(MPa)^{1/2}$ in comparison to parent asphaltene system.

To examine the influence of SBS block copolymer on the bulk properties of graphene-modified asphaltenes, the all-atom MD simulations were carried out for the nanocomposites

Table 4 Comparison of ensemble-averaged bulk properties of the nanocomposites comprising graphene nanosheets (GNS) and asphaltene molecules derived from the 200 ns production MD runs under NPT ensemble

Nanocomposites		ρ (g/cm^3)	E_{coh} (kcal/mol)	δ_{Hild} $(MPa)^{1/2}$	$\delta_{Han/vdW}$ $(MPa)^{1/2}$	$\delta_{Han/Elec}$ $(MPa)^{1/2}$	ΔH_{vap} (kcal/mol)
GNS-A1	Avg	**1.27**	**44.35**	**20.37**	**20.10**	**3.33**	**44.94**
	SD	0.005	0.241	0.089	0.084	0.180	0.241
GNS-A2	Avg	**1.30**	**46.52**	**21.04**	**20.34**	**5.37**	**47.12**
	SD	0.005	0.208	0.075	0.074	0.084	0.208
GNS-A3	Avg	**1.31**	**41.21**	**22.58**	**21.31**	**7.47**	**41.80**
	SD	0.007	0.244	0.113	0.122	0.158	0.244

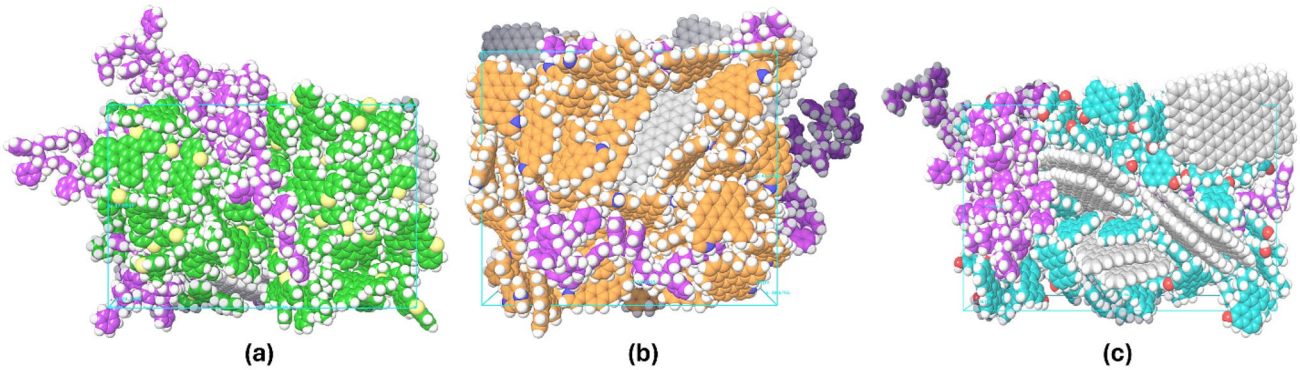

Fig. 4 Equilibrium geometries of the nanocomposites comprising graphene nanosheets (GNS), asphaltene molecules, and SBS block copolymer: **a** GNS-A1/SBS, **b** GNS-A2/SBS, and **c** GNS-A3/SBS, as extracted from the 200 ns NPT MD simulations

consisting of GNS, asphaltenes, and SBS polymer chains. The equilibrium geometries of the SBS-modified GNS-asphaltene nanocomposites accumulated from the 200 ns NPT MD simulations are depicted in Fig. 4. The computed ensemble-averaged bulk properties of such nanocomposites are compared in Table 5. The unsaturated thermoplastic polymer like SBS usually enhances the elastic recovery capacities of the asphalt as well as improves its viscosity, cohesive strength, and ductility. The estimated bulk properties of the SBS-modified GNS-asphaltene nanocomposites show that the density of the graphene-modified asphaltenes is reduced by the addition of SBS polymer chains, which may contribute to increasing the elastic recovery capacities of the material. After the addition of SBS block copolymer, the densities of the graphene-reinforced asphaltenes are found to be comparable with the pristine asphaltene systems (Tables 3 and 5). On the other hand, the improvement of the cohesive strength with the inclusion of polymer is substantiated by the predicted values of E_{coh}. Like the graphene-reinforced asphaltenes, the cohesive strength of the SBS-modified graphene-asphaltene nanocomposites follows the order: GNS-A2/SBS > GNS-A1/SBS > GNS-A3/SBS. The E_{coh} of the SBS-modified nanocomposites is further augmented by about 5.41%, 5.97%, and 1.92%, respectively, for the A1, A2, and A3 asphaltenes compared to their graphene-reinforced systems (Tables 4 and 5). Moreover, the addition of SBS polymer also enhances the compatibility between the graphene nanostructures and the asphaltene molecules, as evidenced by the calculated solubility parameters. The predicted Hildebrand and Hansen solubility parameters of the SBS-modified graphene-asphaltene nanocomposites are very close to the values estimated for the parent asphaltene systems. Usually, materials with comparable δ_d, δ_p, and δ_h with respect to the asphalt components are more compatible in the liquid mixture, while the large deviation of the solubility parameters may lead to phase separation. The calculated $\delta_{Han/Elec}$ and $\delta_{Han/vdW}$ components indicate that the binding of SBS polymer chains with the graphene-reinforced asphaltenes is predominantly guided by the vdW interactions.

To measure the extent of interfacial adhesion between graphene nanosheets and asphaltenes, the classical MD simulations are performed for the model systems of asphaltene molecules together with infinite graphene sheets i.e., periodic graphene layers. Figure 5 shows the thermally equilibrated structures of the graphene-asphaltene interfaces. The computed bulk properties of the PMG-reinforced asphaltene systems as extracted from the production MD runs are reported in Table 6. The calculated ensemble-averaged density at 300 K is found to be enhanced by 29.66%, 26.61%, and 34.17%, respectively, for the PMG-A1, PMG-A2, and PMG-A3 interfaces compared to the pristine asphaltene

Table 5 Comparison of ensemble-averaged bulk properties of the SBS-modified GNS-asphaltene nanocomposites extracted from the 200 ns production MD runs under NPT ensemble

Nanocomposites		ρ (g/cm^3)	E_{coh} (kcal/mol)	δ_{Hild} (MPa)$^{1/2}$	$\delta_{Han/vdW}$ (MPa)$^{1/2}$	$\delta_{Han/Elec}$ (MPa)$^{1/2}$	ΔH_{vap} (kcal/mol)
GNS-A1/SBS	Avg	**1.21**	**46.75**	**19.61**	**19.23**	**3.84**	**47.35**
	SD	0.004	0.208	0.073	0.074	0.082	0.208
GNS-A2/SBS	Avg	**1.24**	**49.30**	**20.37**	**19.71**	**5.15**	**49.89**
	SD	0.004	0.199	0.064	0.065	0.083	0.199
GNS-A3/SBS	Avg	**1.22**	**42.00**	**20.87**	**19.67**	**6.98**	**42.60**
	SD	0.004	0.182	0.072	0.072	0.096	0.182

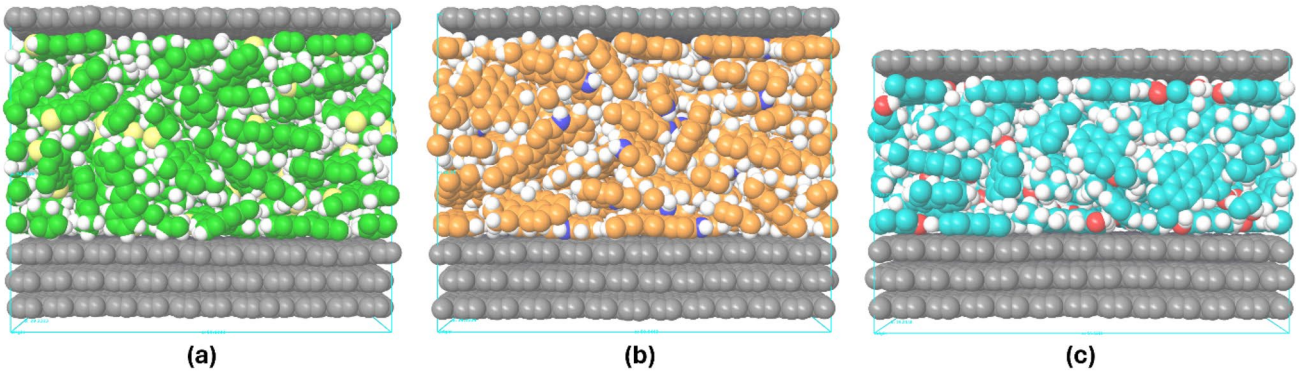

Fig. 5 Equilibrium geometries of the interfaces comprising periodic multilayered graphene (PMG) and asphaltene molecules: **a** PMG-A1, **b** PMG-A2, and **c** PMG-A3, as extracted from the 200 ns NPT MD simulations

materials (Tables 3 and 6). The hierarchical structure of the graphene-asphaltene composites, which is assisted by the stronger π–π stacking interactions, significantly amplifies the cohesive strength compared to the randomly oriented graphene-asphaltene nanocomposites. The values of E_{coh} for the graphene-asphaltene interfaces are raised by about 28.03–31.97 kcal/mol relative to the nanocomposites consisting of finite GNS (Tables 4 and 6). As evidenced by the calculated E_{coh} values, the interfacial interaction intensifies with the size of the aromatic core of the asphaltene molecules. The values of the Hildebrand solubility parameter are also increased by 3.05–3.67 $(MPa)^{1/2}$ for the hierarchical arrangement of the PMG and the asphaltene molecules. The strengthening of vdW interaction at the graphene-asphaltene interfaces compared to the GNS-asphaltene nanocomposites is further supported by the computed dispersion component of the Hansen solubility parameter.

The influence of thermoplastic elastomer on the chemical behavior of graphene-asphaltene interfaces is subsequently explored by conducting all-atom MD simulations for the layered assemblies of graphene, asphaltene, and SBS block copolymer. The equilibrium geometries of the SBS-modified graphene-asphaltene interfaces obtained after the completion of 200 ns production MD runs under the NPT ensemble are represented in Fig. 6. The bulk properties of the SBS-incorporated graphene-asphaltene interfaces as derived from the MD trajectory analyses are displayed in Table 7. The comparison of calculated density values provided in Tables 6 and 7 indicates that the introduction of SBS polymer enhances the structural plasticity of the hierarchical structure of the graphene-asphaltene composites. In addition to that, the cohesive strength between the PMG and the SBS-embedded asphaltenes is boosted by 4.23–10.47%, as manifested by the calculated E_{coh} values. The compatibility between the graphene and asphaltenes is also enhanced after the inclusion of thermoplastic elastomer, which is evidenced by the diminished values of the solubility parameters as estimated for the SBS-modified graphene-asphaltene interfaces. The examination of polar and dispersion components of the Hansen solubility parameter reflects that the vdW interactions play the crucial role in improving the mechanical strength of the nanocomposites.

To elucidate the escalation of cohesive strength between the GNS and the asphaltene molecule comprising N-containing heteroaromatic core (i.e., A2), the quantum chemical calculations are further carried out for a finite model system of GNS-A2 composite as shown in Fig. 7. To capture the quantum effect of the π-electron cloud of the aromatic cores more precisely, the interaction energy is reevaluated by performing DFT-based calculations.

Table 6 Comparison of ensemble-averaged bulk properties of the nanocomposites comprising periodic multilayered graphene nanosheets (PMG) and asphaltene molecules accumulated from the 200 ns production MD runs under NPT ensemble

Nanocomposites		ρ (g/cm^3)	E_{coh} (kcal/mol)	δ_{Hild} $(MPa)^{1/2}$	$\delta_{Han/vdW}$ $(MPa)^{1/2}$	$\delta_{Han/Elec}$ $(MPa)^{1/2}$	ΔH_{vap} (kcal/mol)
PMG-A1	Avg	**1.53**	**73.84**	**23.69**	**23.55**	**2.57**	**74.44**
	SD	0.005	0.215	0.060	0.063	0.130	0.215
PMG-A2	Avg	**1.57**	**78.49**	**24.71**	**24.19**	**5.04**	**79.08**
	SD	0.004	0.219	0.060	0.059	0.077	0.219
PMG-A3	Avg	**1.61**	**69.24**	**25.63**	**24.87**	**6.20**	**69.83**
	SD	0.004	0.222	0.063	0.062	0.153	0.222

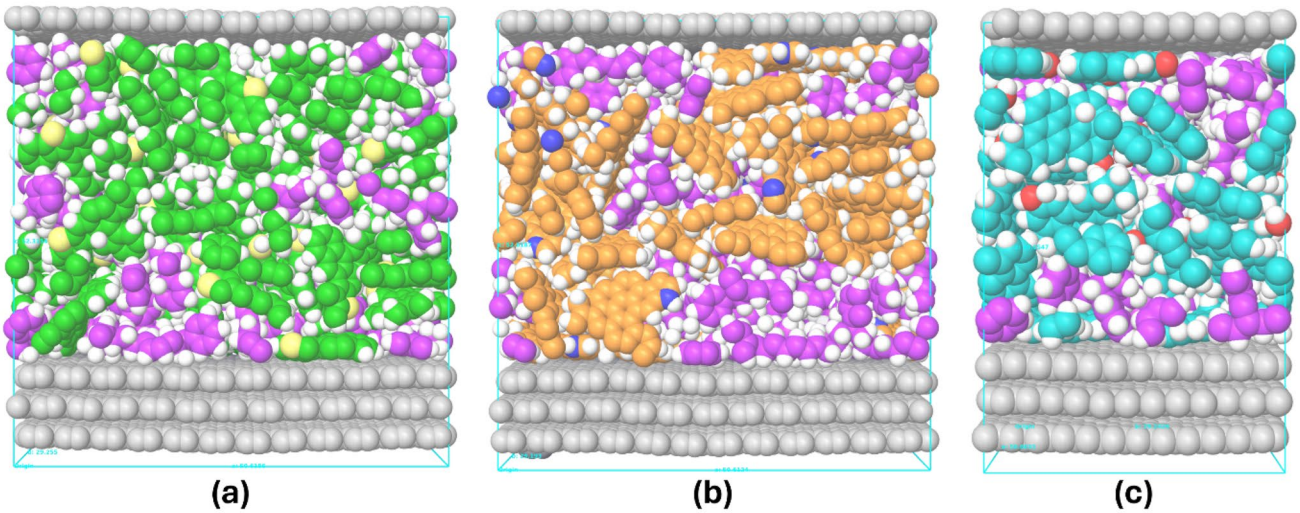

Fig. 6 Equilibrium geometries of the interfaces comprising periodic multilayered graphene (PMG), asphaltene molecules, and SBS block copolymer: **a** PMG-A1/SBS, **b** PMG-A2/SBS, and **c** PMG-A3/SBS, as extracted from the 200 ns NPT MD simulations

Herein, we have employed the dispersion-corrected DFT method to compute the adsorption energy in both the gas phase and solvent medium (toluene). The zero-point energy (ZPE)-corrected electronic energies, as extracted from the DFT calculations at the B3LYP-D3BJ/6-31G(d) level of theory, are used to calculate the adsorption energy,

$$E_a = E(GNS - asphaltene) - [E(GNS) + E(asphaltene)]$$

where E(GNS), E(asphaltene), and E(GNS-asphaltene) refer to the ground state electronic energy of the equilibrium geometries of GNS, asphaltene, and GNS-asphaltene composite, respectively. After the inclusion of ZPE correction, the predicted values of E_a are further rectified by reckoning the basis set superposition error (BSSE). The BSSE correction was invoked by following the counterpoise technique as proposed by Boys and Bernardi [74]. Furthermore, to assess the thermodynamic favorability of the adsorption of asphaltene molecules on the graphene surface, we have calculated changes in enthalpy (ΔH_a) and free energy (ΔG_a) for the surface-molecule interaction in a similar way,

$$\triangle H_a = H(GNS - asphaltene) - [H(GNS) + H(asphaltene)]$$

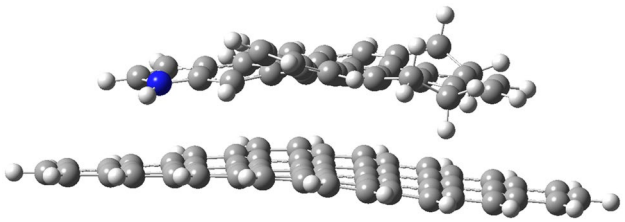

Fig. 7 Optimized structure of the finite model of graphene-asphaltene (GNS-A2) composite, as obtained from the DFT computation at the B3LYP-D3BJ/6-31G(d) level of theory

$$\triangle G_a = G(GNS - asphaltene) - [G(GNS) + G(asphaltene)]$$

The thermal energy correction was included for each structure to predict the thermochemical properties at 298.15 K and 1 atm. The ideal gas, rigid rotor, and harmonic oscillator approximations were considered for computing the translational, rotational, and vibrational contributions to the Gibbs free energy. The predicted trends in adsorption energies before and after the ZPE and BSSE corrections, changes in enthalpy,

Table 7 Comparison of ensemble-averaged bulk properties of the SBS-modified PMG-asphaltene nanocomposites acquired from the 200 ns production MD runs under NPT ensemble

Nanocomposites		ρ (g/cm^3)	E_{coh} (kcal/mol)	δ_{Hild} (MPa)$^{1/2}$	$\delta_{Han/vdW}$ (MPa)$^{1/2}$	$\delta_{Han/Elec}$ (MPa)$^{1/2}$	ΔH_{vap} (kcal/mol)
PMG-A1/SBS	Avg	**1.42**	**79.98**	**22.12**	**21.85**	**3.43**	**80.57**
	SD	0.004	0.259	0.061	0.061	0.081	0.259
PMG-A2/SBS	Avg	**1.41**	**81.81**	**22.28**	**21.72**	**4.95**	**82.41**
	SD	0.001	0.226	0.034	0.035	0.072	0.226
PMG-A3/SBS	Avg	**1.47**	**76.49**	**23.59**	**22.90**	**5.66**	**77.09**
	SD	0.004	0.237	0.061	0.060	0.099	0.237

Table 8 Representation of predicted adsorption energies (E_a) together with ZPE corrected ($E_{a,ZPE}$), and ZPE + BSSE corrected ($E_{a,ZPE+BSSE}$) adsorption energies, enthalpies of adsorption (ΔH_a), and Gibbs free energy changes (ΔG_a) for the adsorption of A2 asphaltene molecule on the surface of graphene nanosheet in both gas and solvent phases at the B3LYP-D3BJ/6-31G(d) level of theory. All the values are in kcal/mol

Medium	E_a	$E_{a,ZPE}$	$E_{a,ZPE+BSSE}$	ΔH_a	ΔG_a
Gas phase	−50.81	−49.13	−36.96	−48.81	−33.41
Solvent phase (toluene)	−49.04	−46.71	−34.63	−46.70	−29.47

and free energy due to the attachment of A2 asphaltene molecule on the surface of GNS in the gas phase and solvent medium are provided in Table 8. The calculated ΔH_a values reveal that the adsorption of asphaltene on the surface of GNS is an exothermic process in both media. As evidenced by the estimated negative values of E_a and ΔG_a, the attachment of asphaltene on the graphene nanostructure is a kinetically and thermodynamically favorable process at once.

Next, we analyzed the simulated IR spectra to reveal the nature of the interaction between the asphaltene and the graphene nanosheet. The computed IR intensities of the GNS, asphaltene (A2), and their composite are depicted in Fig. 8a. The IR spectrum of graphene usually shows no intense peak. However, two major IR peaks appeared at around 910 and 3200 cm^{-1} in the simulated spectrum of graphene crucially originate from the harmonic C-H stretching and out-of-plane C-H bending modes, respectively, associated with terminal H atoms used to passivate the dangling bonds of the finite graphene sheet model. The IR band around 3010–3280 cm^{-1} in the calculated spectrum of asphaltene molecule corresponds to the C-H stretching vibration, while the IR peak located at 3672 cm^{-1} is due to the N–H stretching vibration of the pyrrole moiety attached to the aromatic core of A2. As manifested by the computed IR spectrum of the GNS-A2 composite, the frequency of the important vibrational modes of the pristine materials is not significantly perturbed due to the adsorption of asphaltene molecule onto the graphene surface.

After that, we emphasize the analysis of simulated Raman spectra of the GNS, asphaltene, and their adsorbed complex.

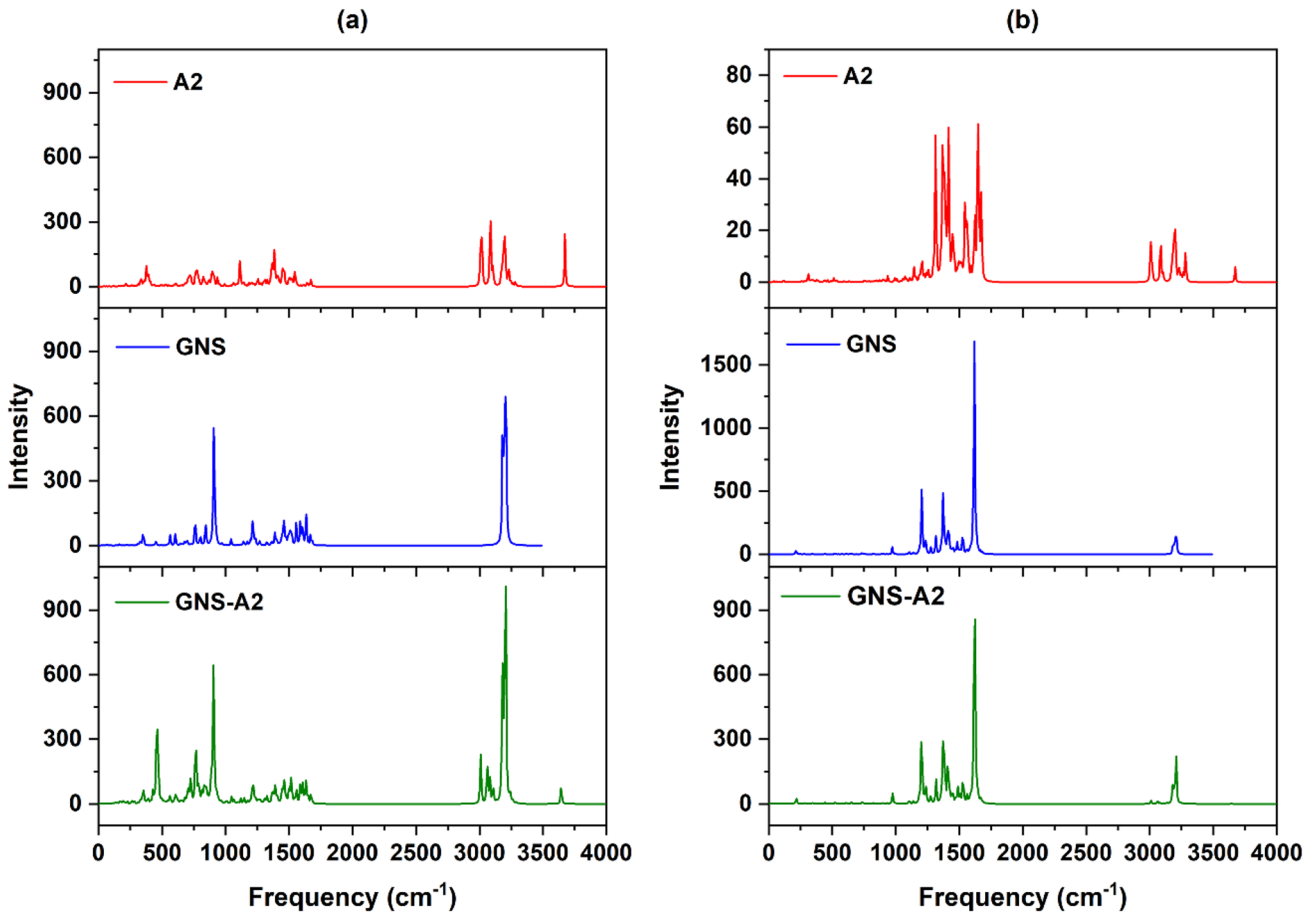

Fig. 8 Comparison of simulated **a** IR and **b** Raman spectra of the GNS-A2 composite, as obtained from the DFT computation at the B3LYP-D3BJ/6-31G(d) level of theory

For each material, the Raman scattering cross-section ($\frac{\partial\sigma}{\partial\Omega}$), which is proportional to the Raman intensity, was estimated as follows:

$$\frac{\partial\sigma_j}{\partial\Omega} = (\frac{2^4\pi^4}{45})(\frac{(\omega_0-\omega_j)^4}{1-\exp(\frac{-hc\omega_j}{kT})})(\frac{h}{8\pi^2 c\omega_j})S_j$$

where ω_j denotes the wavenumber of the *jth* normal mode, ω_0 corresponds to the wavenumber of the Raman excitation line, S_j refers to the scattering activities, and h, c, k are the universal constants. The calculated Raman intensities of asphaltene (A2), GNS, and GNS-A2 composite are compared in Fig. 8b. As revealed by the previous experimental measurement [75], the Raman spectrum of graphene could be differentiated by a D band at 1338 cm^{-1}, a G band at 1578 cm^{-1}, a D′ band at 1615 cm^{-1}, and a 2D band at 2668 cm^{-1}. In the simulated Raman spectrum of GNS, the peaks appeared at 1370, 1618, and 1637 cm^{-1} resemble the experimental D, G, and D′ bands of the graphene, respectively. The calculated 2D band of the graphene is red-shifted compared to the experimental Raman spectrum and is located at around 3208 cm^{-1}. There is no intense Raman band, as manifested by the computed Raman scattering activities for the asphaltene molecule. The characteristic Raman bands of the graphene are retained after the adsorption of asphaltene on the graphene surface. However, the intensity ratio of the D and G band (I_D/I_G) of the graphene is reduced from 0.34 to 0.29 due to the π–π stacking interaction between asphaltene and graphene.

Conclusion

The bulk properties of the model systems of asphaltenes and their nanocomposites reinforced by graphene nanosheets and SBS block copolymer are critically analyzed by performing all-atom classical force field–based MD simulations. The proposed model structures of the asphaltenes comprising heteroatom-substituted aromatic core in conjunction with modified OPLS force field parameters are found to be quite acceptable to reproduce the experimental density and solubility parameters with great accuracy. The addition of graphene nanosheets enhances the cohesive strength of the asphaltenes, and the predicted cohesive energy for the graphene-asphaltene nanocomposites varies between 41.21 and 46.52 kcal/mol. The analysis of Hansen solubility parameters indicates that the interaction of graphene nanostructures with the asphaltene molecules is predominantly guided by the vdW forces. The cohesive strength of the graphene-asphaltene nanocomposites is significantly impacted by the size of the aromatic core and the nature of the heteroatom attached to the aromatic core. The inclusion of SBS block copolymer not only improves the cohesive strength but also recovers the flexibility of the graphene-asphaltene composites. The addition of such polymer is found to be advantageous for enhancing the compatibility of the mixture of nanomaterials and asphaltenes, as substantiated by the proximity between the predicted solubility parameters corresponding to the pristine asphaltenes and the SBS-modified graphene-asphaltene nanocomposites.

The extent of interfacial adhesive strength is probed by analyzing the energetics of the graphene-asphaltene interfaces. The cohesive strength is significantly enhanced by the hierarchical arrangement of the graphene nanosheets and the asphaltene molecules. The cohesive energy of the layered assemblies is augmented by 66.5–68.7% compared to the randomly oriented graphene-asphaltene composites. The energy of cohesion is further strengthened by the inclusion of SBS polymer chains into the graphene-asphaltene matrices. As evidenced by the calculated solubility parameters, the addition of SBS polymer helps to reduce the differences in solubility parameters between the pristine asphaltene and the graphene-reinforced asphaltene systems, which in turn improves the compatibility between components of the interfaces.

The quantum chemical calculations are conducted to reevaluate the energetics of non-covalent interactions between the asphaltene and the graphene nanosheet, within the framework of DFT employing hybrid exchange–correlation functional and integrated schemes including dispersion correction, thermal energy correction, and counterpoise correction. The computed adsorption energies in the gas phase and solvent medium (toluene) support the stronger interactions between the graphene and the asphaltene molecule bearing N-containing larger aromatic core. The DFT-derived thermochemical properties reveal that the adsorption of asphaltene onto the graphene surface is an exothermic and exergonic process. The non-covalent interaction is further substantiated by the retention of characteristic IR and Raman peaks of the graphene and the asphaltene molecule in the simulated spectra of the graphene-asphaltene composite. In summary, the information learned from the ab initio calculations combining classical MD simulations and DFT computations provides crucial structural insight into the binding mechanism of asphaltene, graphene, and thermoplastic polymer, which could pave the way for controlling the asphaltene adsorption capacity using graphene-based adsorbents during heavy-oil refining process and improving the cohesive strength and compatibility of the asphalt binders.

Supplementary Information The online version contains supplementary material available at https://doi.org/10.1007/s11224-024-02330-4.

Acknowledgements The work described in this document was conducted in the Center for Computational Chemistry at Jackson State University. The Authors would like to acknowledge the support provided by the US Army Engineer Research and Development Center

(ERDC) and the Military Engineering Research and Development Area under contract W912HZ-21C0040. Permission to publish was granted by the ERDC Geotechnical and Structures Laboratory. The authors would like to thank Dr. Glake Hill, Professor of Chemistry, Jackson State University, for providing access to computational facilities, especially the Material Science Suite of the Schrödinger code. The authors acknowledge HPC at The University of Southern Mississippi supported by the National Science Foundation under the Major Research Instrumentation (MRI) program via Grant # ACI 1626217.

Author contributions P. N. S. designed the model and the computational framework, performed simulations, and analyzed the data. The first draft of the manuscript was written by P. N. S. and all authors commented on previous versions of the manuscript. D. M. and J. L. conceived the study and were in charge of overall direction and planning. All authors provided critical feedback and helped shape the research, analysis and manuscript.

Funding The financial assistance was provided by the Military Engineering BAA Contract No. W912HZ21C0040, and the Department of Defense (DoD) (Award No. W911NF-21-S-0011). The research described and the resulting data presented herein were funded under CA BO340 497014 Project, "Graphene Applications for Military Engineering," under Contract W912HZ-21C0040, managed by the US Army Engineer Research and Development Center.

Data availability The data that support the findings of this computational study are available from the corresponding author on reasonable request.

Declarations

Competing interests The authors declare no competing interests.

References

1. Schuler B, Zhang Y, Liu F, Pomerantz AE, Andrews AB, Gross L, Pauchard V, Banerjee S, Mullins OC (2020) Overview of asphaltene nanostructures and thermodynamic applications. Energy Fuels 34:15082–15105. https://doi.org/10.1021/acs.energyfuels.0c00874
2. Groenzin H, Mullins OC (2000) Molecular size and structure of asphaltenes from various sources. Energy Fuels 14:677–684. https://doi.org/10.1021/ef990225z
3. McKenna AM, Donald LJ, Fitzsimmons JE, Juyal P, Spicer V, Standing KG, Marshall AG, Rodgers RP (2013) Heavy petroleum composition. 3. Asphaltene Aggregation Energy Fuels 27:1246–1256. https://doi.org/10.1021/ef3018578
4. Hoepfner MP, Fávero CVB, Haji-Akbari N, Fogler HS (2013) The fractal aggregation of asphaltenes. Langmuir 29:8799–8808. https://doi.org/10.1021/la401406k
5. Alshareef AH (2019) Asphaltenes: definition, properties, and reactions of model compounds. Energy Fuels 34:16–30. https://doi.org/10.1021/acs.energyfuels.9b03291
6. Tanaka R, Sato E, Hunt JE, Winans RE, Sato S, Takanohashi T (2004) Characterization of asphaltene aggregates using X-ray diffraction and small-angle X-ray scattering. Energy Fuels 18:1118–1125. https://doi.org/10.1021/ef034082z
7. Bouhadda Y, Bormann D, Sheu E, Bendedouch D, Krallafa A, Daaou M (2007) Characterization of Algerian Hassi-Messaoud asphaltene structure using Raman spectrometry and X-ray diffraction. Fuel 86:1855–1864. https://doi.org/10.1016/j.fuel.2006.12.006
8. Abdallah WA, Yang Y (2012) Raman spectrum of asphaltene. Energy Fuels 26:6888–6896. https://doi.org/10.1021/ef301247n
9. Mullins OC (2010) The modified Yen model. Energy Fuels 24:2179–2207. https://doi.org/10.1021/ef900975e
10. Mullins OC, Sabbah H, Eyssautier J, Pomerantz AE, Barré L, Andrews AB, Ruiz-Morales Y, Mostowfi F, McFarlane RA, Goual L, Lepkowicz R, Cooper TB, Orbulescu J, Leblanc RM, Edwards JE, Zare RN (2012) Advances in asphaltene science and the Yen-Mullins model. Energy Fuels 26:3986–4003. https://doi.org/10.1021/ef300185p
11. Carauta ANM, Correia JCG, Seidl PR, Silva DM (2005) Conformational search and dimerization study of average structures of asphaltenes. J Mol Struct theochem 75:1–8. https://doi.org/10.1016/j.theochem.2005.02.063
12. Mullins OC (2011) The asphaltenes. Annu Rev Anal Chem 4:393–418. https://doi.org/10.1146/annurev-anchem-061010-113849
13. Sedghi M, Goual L, Welch WR, Kubelka J (2013) Effect of asphaltene structure on association and aggregation using molecular dynamics. J Phys Chem B 117:5765–5776. https://doi.org/10.1021/jp401584u
14. Wang H, Xu H, Jia W, Liu J, Ren S (2017) Revealing the intermolecular interactions of asphaltene dimers by quantum chemical calculations. Energy Fuels 31:2488–2495. https://doi.org/10.1021/acs.energyfuels.6b02738
15. Silva HS, Carolina A, Bouyssiere B, Carrier H, Korb J-P, Alfarra A, Vallverdu GS, Bégué D, Baraille I (2016) Molecular dynamics study of nanoaggregation in asphaltene mixtures: effects of the N, O, and S heteroatoms. Energy Fuels 30:5656–5664. https://doi.org/10.1021/acs.energyfuels.6b01170
16. Bian H, Xu F, Kan A, Wei S, Zhang H, Zhang S, Zhu L, Xia D (2021) Insight into the mechanism of asphaltene disaggregation by alkylated treatment: an experimental and theoretical investigation. J Mol Liq 343:117576–117576. https://doi.org/10.1016/j.molliq.2021.117576
17. Ekramipooya A, Valadi FM, Farisabadi A, Gholami MR (2021) Effect of the heteroatom presence in different positions of the model asphaltene structure on the self-aggregation: MD and DFT study. J Mol Liq 334:116109–116109. https://doi.org/10.1016/j.molliq.2021.116109
18. Silva HS, Alfarra A, Vallverdu G, Bégué D, Bouyssiere B, Baraille I (2017) Sensitivity of asphaltene aggregation toward the molecular architecture under desalting thermodynamic conditions. Energy Fuels 32:2681–2692. https://doi.org/10.1021/acs.energyfuels.7b02728
19. Carolina A, Silva H, Level PG, Bouyssiere B, Korb J-P, Carrier H, Alfarra A, Bégué D, Baraille I (2016) Investigation of the effect of sulfur heteroatom on asphaltene aggregation. Energy Fuels 30:4758–4766. https://doi.org/10.1021/acs.energyfuels.6b00757
20. Pacheco-Sánchez JH, Zaragoza IP, Martínez-Magadán JM (2003) Asphaltene aggregation under vacuum at different temperatures by molecular dynamics. Energy Fuels 17:1346–1355. https://doi.org/10.1021/ef020226i
21. Rogel E (2000) Simulation of interactions in asphaltene aggregates. Energy Fuels 14:566–574. https://doi.org/10.1021/ef990166p
22. He L, Wang P, He L, Zhou Q, Luo J, Peng B, Tang X, Pei Y (2018) Molecular dynamics simulations of the self-organization of side-chain decorated polyaromatic conjugation molecules: phase separated lamellar and columnar structures and dispersion behaviors in toluene solvent. RSC Adv 8:11134–11144. https://doi.org/10.1039/c7ra13101a
23. Jian C, Tang T, Bhattacharjee S (2013) Probing the effect of side-chain length on the aggregation of a model asphaltene using molecular dynamics simulations. Energy Fuels 27:2057–2067. https://doi.org/10.1021/ef400097h
24. Martín-Martínez FJ, Fini EH, Buehler MJ (2015) Molecular asphaltene models based on Clar sextet theory. RSC Adv 5:753–759. https://doi.org/10.1039/c4ra05694a

25. Li G, Tan Y (2022) The construction and application of asphalt molecular model based on the quantum chemistry calculation. Fuel 308:122037. https://doi.org/10.1016/j.fuel.2021.122037
26. Headen TF, Boek ES, Skipper NT (2009) Evidence for asphaltene nanoaggregation in toluene and heptane from molecular dynamics simulations. Energy Fuels 23:1220–1229. https://doi.org/10.1021/ef800872g
27. Headen TF, Boek ES, Jackson GL, Totton TS, Müller E (2017) Simulation of asphaltene aggregation through molecular dynamics: insights and limitations. Energy Fuels 31:1108–1125. https://doi.org/10.1021/acs.energyfuels.6b02161
28. Gray MR, Tykwinski RR, Stryker JM, Tan X (2011) Supramolecular assembly model for aggregation of petroleum asphaltenes. Energy Fuels 25:3125–3134. https://doi.org/10.1021/ef200654p
29. Al-Hosani A, Ravichandran S, Daraboina N (2020) Review of asphaltene deposition modeling in oil and gas production. Energy Fuels 35:965–986. https://doi.org/10.1021/acs.energyfuels.0c02981
30. Shoushtari AB, Asadolahpour SR, Madani M (2020) Thermodynamic investigation of asphaltene precipitation and deposition profile in wellbore: a case study. J Mol Liq 320:114468. https://doi.org/10.1016/j.molliq.2020.114468
31. Ahooei A, Norouzi-Apourvari S, Hemmati-Sarapardeh A, Schaffie M (2020) Experimental study and modeling of asphaltene deposition on metal surfaces via electrodeposition process: the role of ultrasonic radiation, asphaltene concentration and structure. J Pet Sci Eng 195:107734–107734. https://doi.org/10.1016/j.petrol.2020.107734
32. Farooq U, Patil A, Panjwani B, Simonsen G (2021) Review on application of nanotechnology for asphaltene adsorption, crude oil demulsification, and produced water treatment. Energy Fuels 35:19191–19210. https://doi.org/10.1021/acs.energyfuels.1c01990
33. Rogel E, Moir ME, Hurt M, Miao T, Lee E (2019) Asphaltene and maltene adsorption into graphene. Energy Fuels 33:9538–9545. https://doi.org/10.1021/acs.energyfuels.9b01681
34. Hosseini-Dastgerdi Z, Meshkat SS (2019) An experimental and modeling study of asphaltene adsorption by carbon nanotubes from model oil solution. J Pet Sci Eng 174:1053–1061. https://doi.org/10.1016/j.petrol.2018.12.024
35. Radnia H, Nazar ARS, Rashidi A (2019) Effect of asphaltene on the emulsions stabilized by graphene oxide: a potential application of graphene oxide in enhanced oil recovery. J Pet Sci Eng 175:868–880. https://doi.org/10.1016/j.petrol.2019.01.034
36. Meshkat SS, Hosseini-Dastgerdi Z, Pakniya F (2023) Asphaltene removal from model oil solution by N doped graphene in a fixed bed column. J Dispers Sci Technol 1–8. https://doi.org/10.1080/01932691.2023.2179491
37. Pensini E, Harbottle D, Yang F, Tchoukov P, Li Z, Kailey I, Behles J, Masliyah J, Xu Z (2014) Demulsification mechanism of asphaltene-stabilized water-in-oil emulsions by a polymeric ethylene oxide–propylene oxide demulsifier. Energy Fuels 28:6760–6771. https://doi.org/10.1021/ef501387k
38. Husain A, Adewunmi AA, Gbadamosi A, Al-Harthi MA, Patil S, Kamal MS (2023) Demulsification of asphaltene stabilized crude oil emulsions by biodegradable ethylcellulose polymers with varying viscosities. Sci Rep 13:1090. https://doi.org/10.1038/s41598-023-27973-x
39. Li X, Ma J, Bian R, Cheng J, Sui H, He L (2020) Novel polyether for efficient demulsification of interfacially active asphaltene-stabilized water-in-oil emulsions. Energy Fuels 34:3591–3600. https://doi.org/10.1021/acs.energyfuels.9b03518
40. Mao X, Wang F, Lu B, Tang T, Liu Q, Zeng H (2023) Novel polymer nanoparticles with core–shell structure for breaking asphaltenes-stabilized W/O and O/W emulsions. J Colloid Interface Sci 640:296–308. https://doi.org/10.1016/j.jcis.2023.02.080
41. Feng X, Xu Z, Masliyah J (2008) Biodegradable polymer for demulsification of water-in-bitumen emulsions. Energy Fuels 23:451–456. https://doi.org/10.1021/ef800825n
42. Wang FH, Shen LB, Zhu H, Han KF (2011) The preparation of a polyether demulsifier modified by nano-SiO_2 and the effect on asphaltenes and resins. Pet Sci Technol 29:2521–2529. https://doi.org/10.1080/10916460903393997
43. Li Z, Fuentes JV, Chakraborty A, Zamora EB, Prasad V, Vázquez F, Xu Z, Liu Q, Flores C, McCaffrey WC (2023) Dehydration of water-in-crude oil emulsions using polymeric demulsifiers: a model for water removal based on the viscoelastic properties of the oil–water interfacial film. Fuel 332:126185–126185. https://doi.org/10.1016/j.fuel.2022.126185
44. Mosleh FM, Mortazavi Y, Hosseinpour N, Khodadadi AA (2019) Asphaltene adsorption onto carbonaceous nanostructures. Energy Fuels 34:211–224. https://doi.org/10.1021/acs.energyfuels.9b03466
45. Lan T, Zeng H, Tang T (2019) Molecular dynamics study on the mechanism of graphene oxide to destabilize oil/water emulsion. J Phys Chem C 123:22989–22999. https://doi.org/10.1021/acs.jpcc.9b05906
46. Liang M, Liang P, Fan W, Qian C, Xin X, Shi J, Nan G (2015) Thermo-rheological behavior and compatibility of modified asphalt with various styrene–butadiene structures in SBS copolymers. Mater Des 88:177–185. https://doi.org/10.1016/j.matdes.2015.09.002
47. Cai HM, Wang T, Zhang JY, Zhang YZ (2010) Preparation of an SBS latex–modified bitumen emulsion and performance assessment. Pet Sci Technol 28:987–996. https://doi.org/10.1080/10916460902939436
48. Abd El-Rahman AMM, El-Shafie M, Abo-Shanab ZL, El-Kholy SA (2017) Modifying asphalt emulsion with different types of polymers for surface treatment applications. Pet Sci Technol 35:1473–1480. https://doi.org/10.1080/10916466.2017.1344709
49. Zhang L, Greenfield ML (2007) Molecular orientation in model asphalts using molecular simulation. Energy Fuels 21:1102–1111. https://doi.org/10.1021/ef060449z
50. Zhang L, Greenfield ML (2010) Rotational relaxation times of individual compounds within simulations of molecular asphalt models. J Chem Phys 132:184502. https://doi.org/10.1063/1.3416913
51. Zhang L, Greenfield ML (2007) Analyzing properties of model asphalts using molecular simulation. Energy Fuels 21:1712–1716. https://doi.org/10.1021/ef060658j
52. Bhasin A, Bommavaram R, Greenfield ML, Little DN (2011) Use of molecular dynamics to investigate self-healing mechanisms in asphalt binders. J Mater Civ Eng 23:485–492. https://doi.org/10.1061/(asce)mt.1943-5533.0000200
53. Li DD, Greenfield ML (2014) Chemical compositions of improved model asphalt systems for molecular simulations. Fuel 115:347–356. https://doi.org/10.1016/j.fuel.2013.07.012
54. Li DD, Greenfield ML (2011) High internal energies of proposed asphaltene structures. Energy Fuels 25:3698–3705. https://doi.org/10.1021/ef200507c
55. Lu C, Wu C, Ghoreishi D, Chen W, Wang L, Damm W, Ross GA, Dahlgren MK, Russell E, Von Bargen CD, Abel R, Friesner RA, Harder ED (2021) OPLS4: improving force field accuracy on challenging regimes of chemical space. J Chem Theory Comput 17:4291–4300. https://doi.org/10.1021/acs.jctc.1c00302
56. Nosé S (1984) A unified formulation of the constant temperature molecular dynamics methods. J Chem Phys 81:511–519. https://doi.org/10.1063/1.447334
57. Nosé S (1984) A molecular dynamics method for simulations in the canonical ensemble. Mol Phys 52:255–268. https://doi.org/10.1080/00268978400101201

58. Hoover WG (1985) Canonical dynamics: equilibrium phase-space distributions. Phys Rev A 31:1695–1697. https://doi.org/10.1103/physreva.31.1695
59. Martyna GJ, Tobias DJ, Klein ML (1994) Constant pressure molecular dynamics algorithms. J Chem Phys 101:4177–4189. https://doi.org/10.1063/1.467468
60. Bowers KJ, Sacerdoti FD, Salmon JK, Shan Y, Shaw DE, Chow E, Xu H, Dror RO, Eastwood MP, Gregersen BA, Klepeis JL, Kolossvary I, Moraes MA (2006) Molecular dynamics scalable algorithms for molecular dynamics simulations on commodity clusters. Proceedings of the 2006 ACM/IEEE conference on Supercomputing - SC '06. https://doi.org/10.1145/1188455.1188544
61. Becke AD (1993) Density-functional thermochemistry. III. The role of exact exchange. J Chem Phys 98:5648–5652. https://doi.org/10.1063/1.464913
62. Vosko SH, Wilk L, Nusair M (1980) Accurate spin-dependent electron liquid correlation energies for local spin density calculations: a critical analysis. Can J Phys 58:1200. https://doi.org/10.1139/p80-159
63. Lee C, Yang W, Parr RG (1988) Development of the Colle-Salvetti correlation-energy formula into a functional of the electron density. Phys Rev B 37:785–789. https://doi.org/10.1103/physrevb.37.785
64. Grimme S, Ehrlich S, Goerigk L (2011) Effect of the damping function in dispersion corrected density functional theory. J Comput Chem 32:1456–1465. https://doi.org/10.1002/jcc.21759
65. Miertuš S, Scrocco E, Tomasi J (1981) Electrostatic interaction of a solute with a continuum. A direct utilizaion of AB initio molecular potentials for the prevision of solvent effects. Chem Phys 55:117–129. https://doi.org/10.1016/0301-0104(81)85090-2
66. Tomasi J, Mennucci B, Cammi R (2005) Quantum mechanical continuum solvation models. Chem Rev 105:2999–3094. https://doi.org/10.1021/cr9904009
67. Barone V, Cossi M, Tomasi J (1998) Geometry optimization of molecular structures in solution by the polarizable continuum model. J Comput Chem 19:404–417. https://doi.org/10.1002/(sici)1096-987x(199803)19:4%3C404::aid-jcc3%3E3.0.co;2-w
68. Frisch MJ, Trucks GW, Schlegel HB, Scuseria GE, Robb MA, Cheeseman JR, Scalmani G, Barone V, Petersson GA, Nakatsuji H, Li X, Caricato M, Marenich AV, Bloino J, Janesko BG, Gomperts R, Mennucci B, Hratchian HP, Ortiz JV, Izmaylov AF, Sonnenberg JL, Williams, Ding F, Lipparini F, Egidi F, Goings J, Peng B, Petrone A, Henderson T, Ranasinghe D, Zakrzewski VG, Gao J, Rega N, Zheng G, Liang W, Hada M, Ehara M, Toyota K, Fukuda R, Hasegawa J, Ishida M, Nakajima T, Honda Y, Kitao O, Nakai H, Vreven T, Throssell K, Montgomery Jr. JA, Peralta JE, Ogliaro F, Bearpark MJ, Heyd JJ, Brothers EN, Kudin KN, Staroverov VN, Keith TA, Kobayashi R, Normand J, Raghavachari K, Rendell AP, Burant JC, Iyengar SS, Tomasi J, Cossi M, Millam JM, Klene M, Adamo C, Cammi R, Ochterski JW, Martin RL, Morokuma K, Farkas O, Foresman JB, Fox DJ, 2016, Gaussian 16 Rev. C.01, Wallingford, CT
69. Elkahky S, Lagat C, Sarmadivaleh M, Barifcani A (2019) A comparative study of density estimation of asphaltene structures using group contribution methods and molecular dynamic simulations for an Australian oil field. J Pet Explor Prod Technol 9:2699–2708. https://doi.org/10.1007/s13202-019-0641-x
70. Hildebrand JH (1936) Solubility of non-electrolytes. Reinhold Publishing Corporation, New York
71. Hansen CM (1969) The universality of the solubility parameter. Ind Eng Chem Prod Res Dev 8:2–11. https://doi.org/10.1021/i360029a002
72. Redelius P (2004) Bitumen solubility model using hansen solubility parameter. Energy Fuels 18:1087–1092. https://doi.org/10.1021/ef0400058
73. Zhang L, Greenfield ML (2008) Effects of polymer modification on properties and microstructure of model asphalt systems. Energy Fuels 22:3363–3375. https://doi.org/10.1021/ef700699p
74. Boys SF, Bernardi F (1970) The calculation of small molecular interactions by the differences of separate total energies. Some procedures with reduced errors. Mol Phys 19:553–566. https://doi.org/10.1080/00268977000101561
75. Rao KS, Senthilnathan J, Liu Y-F, Yoshimura M (2014) Role of peroxide ions in formation of graphene nanosheets by electrochemical exfoliation of graphite. Sci Rep 4:4237. https://doi.org/10.1038/srep04237